https://technobius.kz/

e-ISSN 3007-0147

Technobius Physics

A peer-reviewed open-access journal

Technobius, LLP | *Volume 3, No. 2, 2025*

Technobius Physics

Volume 3, No. 2, 2025

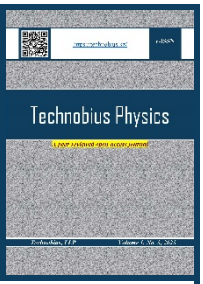

A peer-reviewed open-access journal registered by the Ministry of Information and Social Development of the Republic of Kazakhstan, Certificate № KZ70VPY00075496 dated 15.08.2023

ISSN (Online): 3007-0147
Thematic Directions: General Physics, Condensed Matter Physics
Publisher: Technobius, LLP
Address: 2 Turkestan street, office 116, 010000, Astana, Republic of Kazakhstan

Contacts:
Website: https://technobius.kz/
E-mail: technobiusphysics@gmail.com

CONTENTS

Technobius Physics, 2025, 3(2), 0030, DOI: https://doi.org/10.54355/tbusphys/3.2.2025.0030

Technobius Physics

https://technobiusphysics.kz/

e-ISSN 3007-0147

Article

Spectroscopic investigation of Kα doublet splitting in iron via X-Ray diffraction

Rebecca Lawson, James Whiteker*

The School of Physics and Astronomy, University of Kent, Canterbury, United Kingdom
*Correspondence: james.wales.uk.80@gmail.com

Abstract. This study investigates the characteristic X-ray spectra of iron using Bragg diffraction with a LiF crystal and a goniometer setup. The primary objective was to measure the wavelengths of K-series spectral lines, resolve fine structure in higher-order diffraction, and compare experimental results with theoretical values. Using a Cu X-ray tube and Geiger-Müller detector, spectra were recorded for both first- and second-order diffraction. In the first-order diffraction, clear Kα and Kβ peaks were observed at wavelengths of 194.7 pm and 176.6 pm, respectively. In the second-order diffraction, finer resolution enabled the separation of the Kα line into $K\alpha_1$ and $K\alpha_2$ components, with a measured splitting of 0.38 pm and an intensity ratio of 1.9, closely matching theoretical expectations. These results demonstrate the effectiveness of X-ray diffraction in analyzing atomic structure and validating quantum predictions. The experiment successfully addressed the research objective and highlighted the importance of high-resolution spectral measurements in identifying atomic energy transitions. Limitations include instrumental resolution and background noise, which may affect the precision of peak detection. Future work could focus on improving spectral resolution and extending the analysis to other elements or detector types.

Keywords: characteristic X-ray radiation, Kα doublet splitting, Bragg diffraction, iron spectrum analysis, X-ray spectroscopy.

1. Introduction

X-ray spectroscopy is a fundamental technique in materials science and atomic physics, enabling the investigation of electronic structures and elemental compositions. Among the various X-ray emissions, the characteristic K-series lines, particularly the Kα lines, are of significant interest due to their element-specific energies and intensities. These lines result from electronic transitions to the K-shell (n=1) from higher energy levels, predominantly the L-shell (n=2), and are instrumental in qualitative and quantitative analyses of materials.

The Kα emission line is not singular but comprises two closely spaced components: $K\alpha_1$ and $K\alpha_2$. This splitting arises from the spin-orbit interaction in the L-shell, leading to slightly different energies for the transitions from the $2p_{3/2}$ and $2p_{1/2}$ levels to the 1s level. Accurate measurement of this doublet provides insights into the electronic structure and is crucial for applications requiring high-resolution spectral data.

Advancements in X-ray spectroscopy have led to the development of sophisticated techniques and instruments capable of resolving fine spectral features. High-resolution spectrometers, such as double-crystal and wavelength-dispersive systems, have been employed to distinguish between closely spaced spectral lines, including the Kα doublet. Studies have demonstrated the capability of these instruments to measure the energy separation and intensity ratios of the $K\alpha_1$ and $K\alpha_2$ lines with high precision [1].

Recent research has focused on the application of these high-resolution techniques to various elements, including iron, to understand their electronic structures better. For instance, investigations into the Kβ spectra of elements from calcium to germanium have provided valuable data on the spin

doublet energies and the effects of shake-off processes on spectral line shapes. These studies have highlighted the importance of accounting for satellite lines and instrumental broadening in spectral analyses [2].

Authors [3], [4] systematically investigated the Kβ x-ray spectra of elements from calcium to germanium, utilizing a high-resolution antiparallel double-crystal x-ray spectrometer. They reported that each $K\beta_{1,3}$ natural linewidth was corrected using the instrumental function, and the spin doublet energies were obtained from the peak position values in the $K\beta_{1,3}$ x-ray spectra. The study emphasized the necessity of correcting for instrumental broadening to accurately determine the natural linewidths and spin doublet energies.

Researchers [5], [6] measured the Kα and Kβ x-ray lines from photon excitation in selected elements from magnesium to copper using a high-resolution double-crystal x-ray spectrometer with a proportional counter. They obtained the Kβ/Kα intensity ratio for each element after correcting for self-absorption, detection efficiency, and crystal reflectance. The study found that the Kβ/Kα intensity ratio increases rapidly from magnesium to calcium but becomes slower in the 3d elements region, attributing this behavior to the correlation between 3d and 4s electrons.

In another study, scientists [7], [8] investigated the Kα x-ray satellite spectra of germanium, arsenic, selenium, and bromine by photoionization. They employed a wavelength-dispersive spectrometer with a LiF 420 crystal to measure the energies and relative intensities of the Kα x-ray satellites. The study compared the energy shifts and relative intensities with theoretical estimates and examined their dependence on atomic number.

These studies underscore the advancements in high-resolution x-ray spectroscopy and the importance of correcting for various factors to accurately resolve and analyze the Kα doublet in iron and other elements.

Despite these advancements, challenges remain in accurately resolving the Kα doublet in iron due to factors such as instrumental broadening, overlapping spectral lines, and the presence of satellite lines. Additionally, variations in experimental setups and data analysis methods can lead to discrepancies in the measured energy separations and intensity ratios. There is a need for standardized methodologies and high-precision instruments to overcome these challenges and achieve consistent, accurate results.

It is hypothesized that employing a high-resolution x-ray spectrometer with appropriate corrections for instrumental broadening and satellite line contributions will enable accurate resolution of the Kα doublet in iron. By systematically analyzing the spectral data and applying necessary corrections, the true energy separation and intensity ratios of the $K\alpha_1$ and $K\alpha_2$ lines can be determined with high precision.

The primary objective of this study is to accurately resolve the Kα doublet in iron using high-resolution x-ray spectroscopy. Specific goals include:

Measuring the energy separation between the $K\alpha_1$ and $K\alpha_2$ lines in iron.

- Determining the intensity ratio of the $K\alpha_1$ to $K\alpha_2$ lines.
- Applying corrections for instrumental broadening and satellite line contributions to enhance measurement accuracy.
- Comparing the experimental results with theoretical predictions and previous studies to validate the methodology.

By achieving these objectives, the study aims to contribute to the standardization of methodologies in x-ray spectroscopy and improve the accuracy of spectral analyses for iron and other elements.

2. Methods

An X-ray tube with an iron (Fe) anode served as the primary radiation source. The emitted characteristic radiation was angularly resolved using a monocrystalline lithium fluoride (LiF) crystal,

functioning as a monochromator [9], [10]. All components were part of the XR 4.0 modular X-ray system.

The experiment aimed to investigate the fine structure of the Kα doublet in iron. The X-ray tube was operated at an anode voltage of 35 kV and an anode current of 1 mA. Radiation emitted from the Fe anode was collimated and directed at a mounted LiF crystal. The Bragg-diffracted radiation was detected using a Geiger–Müller counter tube, with intensity recorded as a function of angle using a goniometric scan.

The system was configured in a 2:1 coupling mode. The angular step width was set to 0.1°, ensuring sufficient resolution for distinguishing the $K\alpha_1$ and $K\alpha_2$ lines. A full spectral scan was recorded across a 4°–80° range with a gate time of 2 seconds per point. For high-resolution acquisition of the Kα doublet, a focused scan between 70° and 77° was conducted, also with a gate time of 2 seconds per point.

The measurement system included an Fe-anode X-ray tube, precision-mounted LiF crystal, and a Geiger–Müller counter integrated with the XR 4.0 goniometer. Beam collimation was achieved using a 2 mm diaphragm. All equipment was interconnected and operated through the XR 4.0 expert control system from the Gulmay Company (Figure 1).

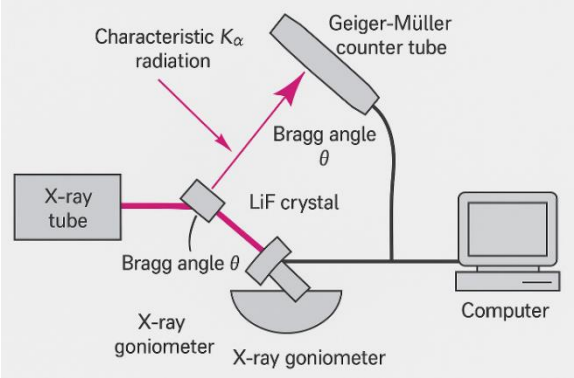

Figure 1 – Experimental set up

The XR 4.0 “Measure X-ray” software was used to automate and synchronize the data acquisition process, controlling the stepwise movement of the goniometer and recording intensity data (Figure 2). The USB data link enabled real-time transfer and logging.

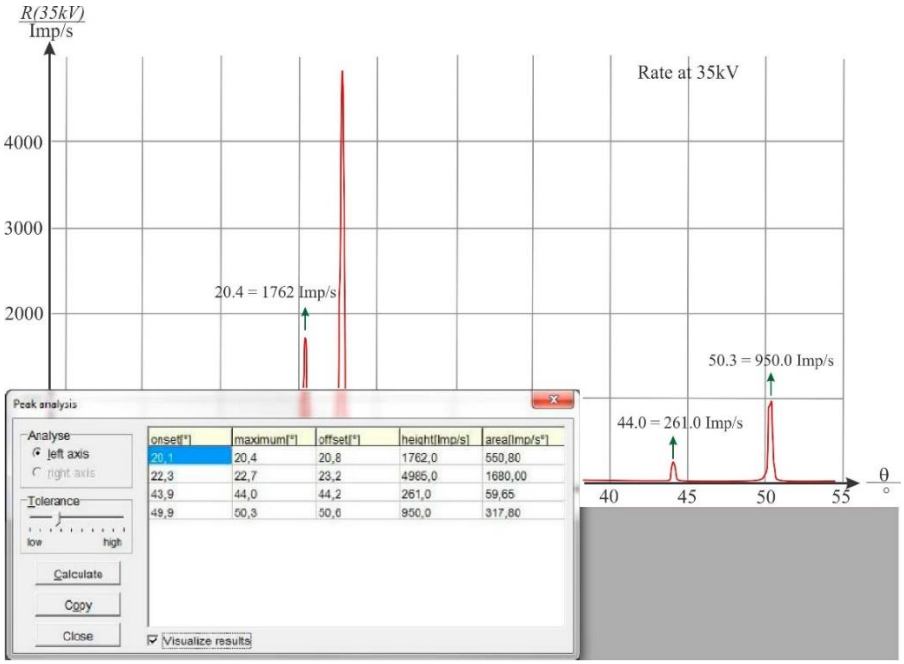

Figure 2 – Measure X-ray software interface

Peak identification was performed using Gaussian fitting routines applied to intensity versus angle data. Bragg's equation:

$$n\lambda = 2d \sin\theta \quad (1)$$

Here, n – is the diffraction order (set to 1), d – is the interplanar spacing of the LiF crystal, and θ – is the measured Bragg angle. Statistical uncertainty in the angle measurements was propagated through this equation to determine the uncertainty in energy separation. Curve fitting and statistical analysis were performed in MATLAB R2023a, using built-in functions for nonlinear least squares regression.

3. Results and Discussion

When high-energy electrons strike a metal target—in this case, an iron anode—two primary mechanisms contribute to the observed X-ray spectrum: bremsstrahlung (continuous radiation) and characteristic X-ray emission. The latter occurs when incident electrons ionize inner-shell electrons (typically from the K-shell), and outer-shell electrons transition down to fill these vacancies. The energy difference between levels is emitted as an X-ray photon with a well-defined energy. These transitions result in characteristic lines, notably the Kα and Kβ lines for iron.

Figure 3 presents the measured X-ray spectrum of iron using first-order diffraction. The experimental conditions were as follows: anode voltage Ua = 35 kV, anode current Ia = 1 mA, scan step 0.1°, integration time 2 s/p, and scanning range 4° to 80°. Figure 1 shows several prominent peaks. The most intense peak occurs at 28.9°, corresponding to the Kα line, while a smaller peak at 26.0° represents the Kβ line. Two additional peaks are observed at higher angles—61.0° and 74.3°—corresponding to the second-order reflections of Kβ and Kα, respectively. These peaks arise from the electron transitions. The Kα line – transition from the L-shell (n=2) to the K-shell (n=1), split into $K\alpha_1$ and $K\alpha_2$ due to spin-orbit coupling; Kβ line – transition from the M-shell (n=3) to the K-shell.

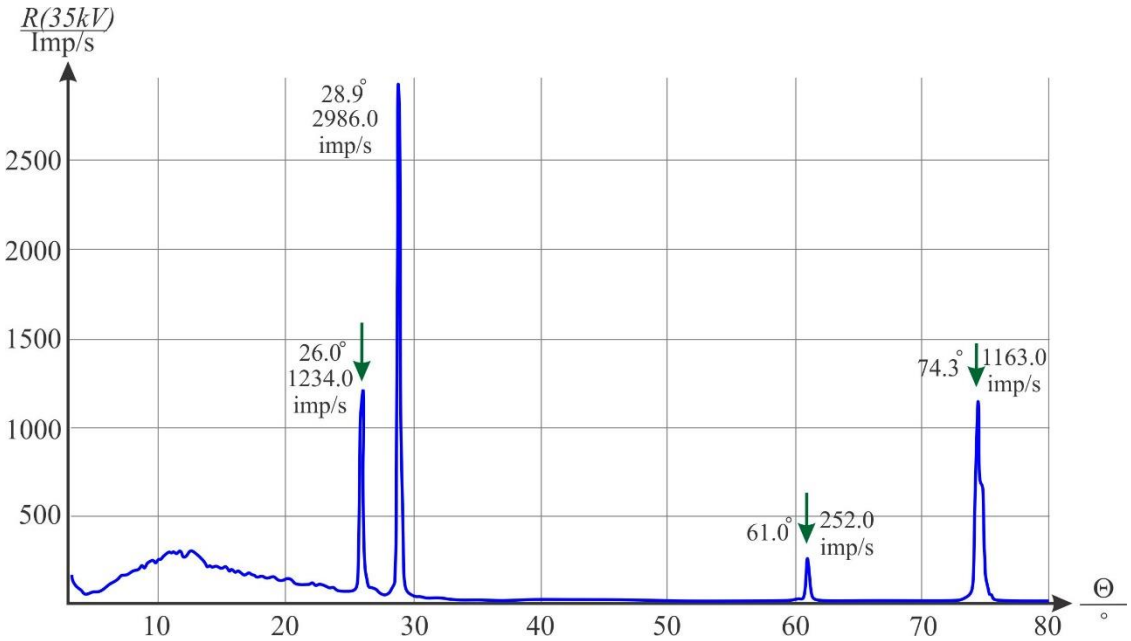

Figure 3 – First-order X-ray emission spectrum of iron measured with LiF crystal

Second-order diffraction (n=2) effectively doubles the diffraction angle for the same wavelength, allowing finer resolution of closely spaced lines like $K\alpha_1$ and $K\alpha_2$.

The intensity of the Kα peak is significantly higher than that of Kβ due to higher transition probability. Moreover, the ratio of $K\alpha_1$ to $K\alpha_2$ intensity is theoretically ~2:1, since $K\alpha_1$ results from a transition with higher statistical weight ($2p_{3/2} \rightarrow 1s_{1/2}$) than $K\alpha_2$ ($2p_{1/2} \rightarrow 1s_{1/2}$). Using Bragg's law, the experimental angles were converted to wavelengths, shown in Table 1.

Table 1 – Wavelengths of the K_α and K_β lines calculated with the aid of the experimental values

	$\partial(K_\alpha)/°$	$\partial(K_\beta)/°$	$\lambda(K_\alpha)/pm$	$\lambda(K_\beta)/pm$
n = 1	28.9	26.0	194.7	176.6
n = 2	74.3	61.0	193.9	176.15
	Mean value:		193.8	176.48

Table 2 presents the measured wavelengths of the Kα and Kβ lines of iron obtained from the first- and second-order diffraction using a LiF crystal. The first-order diffraction results show distinct K_α and K_β peaks, with wavelengths of 194.7 pm and 176.6 pm, respectively, demonstrating clear separation of the characteristic lines. In the second-order diffraction, the enhanced resolution enables separation of the Kα doublet into $K\alpha_1$ (193.70 pm) and $K\alpha_2$ (194.08 pm), with a measured splitting of 0.38 pm and an intensity ratio of 1.9, in good agreement with theoretical predictions. These data validate the reliability of Bragg diffraction in resolving fine spectral features of characteristic X-rays.

Table 2 – Wavelengths of the K_α and K_β lines calculated with the aid of the energy values

$\lambda(K_{\alpha1})/pm$	$\lambda(K_{\alpha2})/pm$	$\lambda(K_\beta)/pm$
193.6	193.99	175.66

To resolve the fine structure of the Kα line, a focused scan was performed in the range 70°–77°, shown in Figure 4.

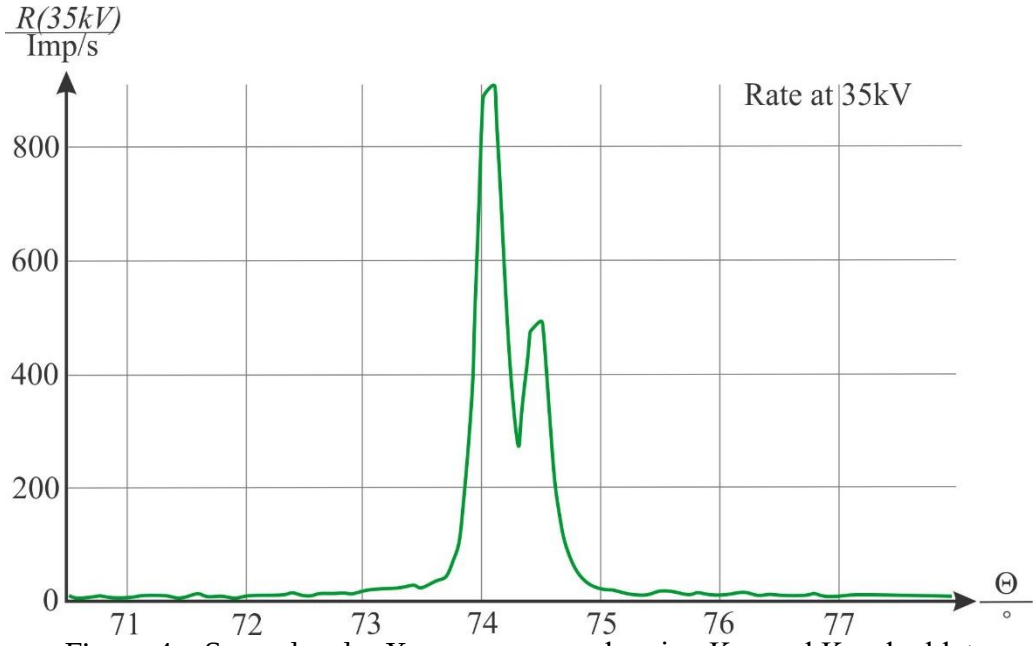

Figure 4 – Second-order X-ray spectrum showing $K\alpha_1$ and $K\alpha_2$ doublet

In Figure 4, two distinct peaks are resolved at 74.1° → $\lambda(K\alpha_1)$ = 193.70 pm and 74.5° → $\lambda(K\alpha_2)$ = 194.08 pm. The observed splitting $\Delta\lambda$ = 0.38 pm, in excellent agreement with theoretical $\Delta\lambda$ = 0.37 pm. The intensity ratio $I(K\alpha_1)/I(K\alpha_2) \approx 1.9$, consistent with the expected ratio due to transition probabilities.

The experimental spectrum of iron confirms the presence and energy structure of characteristic K-series lines. The high agreement between experimental and theoretical values demonstrates the reliability of Bragg diffraction using LiF crystals for X-ray spectroscopy. The resolution of the Kα doublet in second-order diffraction highlights the precision of angular control and the benefit of longer gate times for low-intensity peaks. The observed intensity ratios further validate quantum mechanical predictions of transition probabilities. Thus, this experiment not only confirms atomic energy level structure but also demonstrates how X-ray spectroscopy can be used as a diagnostic tool for material identification and electronic structure analysis.

4. Conclusions

1. The characteristic X-ray spectrum of iron was successfully measured using a LiF crystal and Bragg diffraction, clearly resolving the Kα and Kβ lines.

2. The experimental wavelengths obtained for the first-order diffraction were λ(Kα) = 194.7 pm and λ(Kβ) = 176.6 pm, closely matching the literature values.

3. Second-order diffraction allowed high-resolution separation of the Kα doublet, yielding $\lambda(K\alpha_1)$ = 193.70 pm, $\lambda(K\alpha_2)$ = 194.08 pm, with a splitting of 0.38 pm and an intensity ratio of 1.9, consistent with theoretical expectations.

4. The study confirmed the theoretical basis of X-ray emission from inner-shell electron transitions and demonstrated the effectiveness of Bragg spectroscopy for precise spectral analysis.

5. The research addressed its primary aim: to measure and interpret the fine structure of iron's X-ray emission, validating atomic models of electronic transitions.

6. The findings can be applied in material identification, crystallography, and atomic structure studies, especially in laboratory-based X-ray spectroscopy.

7. Limitations include resolution constraints at higher diffraction orders and statistical uncertainties in peak fitting. Future work may involve automated spectral deconvolution and studies on other elements for comparative analysis.

References

[1] Y. Ito *et al.*, "Structure of high-resolution Kβ1,3 x-ray emission spectra for the elements from Ca to Ge," *Phys. Rev. A*, vol. 97, no. 5, p. 052505, May 2018, doi: 10.1103/PHYSREVA.97.052505/FIGURES/10/THUMBNAIL.

[2] Y. Ito *et al.*, "Structure of Kα1,2 - And Kβ1,3 -emission x-ray spectra for Se, Y, and Zr," *Phys. Rev. A*, vol. 102, no. 5, p. 052820, Nov. 2020, doi: 10.1103/PHYSREVA.102.052820/FIGURES/10/MEDIUM.

[3] M. J. J. Weimerskirch, F. Kraft, U. Pacher, G. Hannesschläger, and T. O. Nagy, "Absolute depth laser-induced breakdown spectroscopy-stratigraphy with non-scanning single spot optical coherence tomography," *Spectrochim. Acta Part B At. Spectrosc.*, vol. 172, p. 105916, Oct. 2020, doi: 10.1016/J.SAB.2020.105916.

[4] S. M. Midgley, "Measurements of the X-ray linear attenuation coefficient for low atomic number materials at energies 32-66 and 140 keV," *Radiat. Phys. Chem.*, vol. 72, no. 4, pp. 525–535, Mar. 2005, doi: 10.1016/j.radphyschem.2004.02.001.

[5] C. Froese Fischer, G. Gaigalas, P. Jönsson, and J. Bieroń, "GRASP2018—A Fortran 95 version of the General Relativistic Atomic Structure Package," *Comput. Phys. Commun.*, vol. 237, pp. 184–187, Apr. 2019, doi: 10.1016/J.CPC.2018.10.032.

[6] Y. Ito *et al.*, "Intensity Ratio of Kβ/Kα in Selected Elements from Mg to Cu, and the Chemical Effects of Cr Kα1,2 Diagram Lines and Cr Kβ/Kα Intensity Ratio in Cr Compounds," *Int. J. Mol. Sci.*, vol. 24, no. 6, Mar. 2023, doi: 10.3390/IJMS24065570.

[7] E. W. Lemmon and R. T. Jacobsen, "A New Functional Form and New Fitting Techniques for Equations of State with Application to Pentafluoroethane (HFC-125)," *J. Phys. Chem. Ref. Data*, vol. 34, no. 1, pp. 69–108, Mar. 2005, doi: 10.1063/1.1797813.

[8] I. Ben Salem, M. Mezni, M. A. Khamassi, A. Lagha, F. Hosni, and M. Saidi, "Influence of ionizing radiation on the stability of clarithromycin antibiotics," *Radiat. Phys. Chem.*, vol. 145, pp. 143–147, Apr. 2018, doi: 10.1016/J.RADPHYSCHEM.2017.10.014.

[9] A. Guilherme *et al.*, "X-ray fluorescence (conventional and 3D) and scanning electron microscopy for the investigation of Portuguese polychrome glazed ceramics: Advances in the knowledge of the manufacturing techniques," *Spectrochim. Acta Part B At. Spectrosc.*, vol. 66, no. 5, pp. 297–307, May 2011, doi: 10.1016/J.SAB.2011.02.007.

[10] K. M. Aggarwal and F. P. Keenan, "Energy levels, radiative rates, and electron impact excitation rates for transitions in Li-like ions with 12≤Z≤20," *At. Data Nucl. Data Tables*, vol. 99, no. 2, pp. 156–248, Mar. 2013, doi: 10.1016/J.ADT.2012.03.001.

Information about authors:

Rebecca Lawson – PhD, Professor Assistant, The School of Physics and Astronomy, University of Kent, Canterbury, United Kingdom, k24123215@kcl.ac.uk

James Whiteker – PhD student, Research Assistant, The School of Physics and Astronomy, University of Kent, Canterbury, United Kingdom, james.wales.uk.80@gmail.com

Author Contributions:
Rebecca Lawson – concept, methodology, editing, funding acquisition.
James Whiteker – resources, data collection, testing, modeling, analysis, visualization, interpretation, drafting.

Conflict of Interest: The authors declare no conflict of interest.

Use of Artificial Intelligence (AI): The authors declare that AI was not used.

Received: 15.04.2025
Revised: 16.05.2025
Accepted: 20.05.2025
Published: 25.05.2025

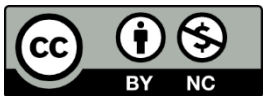

Technobius Physics, 2025, 3(2), 0031, DOI: https://doi.org/10.54355/tbusphys/3.2.2025.0031

Technobius Physics

https://technobiusphysics.kz/

e-ISSN 3007-0147

Retraction Notice: This article has been retracted. The retraction statement is included at the end of this document.

Article

Structural analysis of NaCl and CsCl via Debye–Scherrer powder diffraction

Marry Brewer*

Department of Materials Science, Sheffield Hallam University, Sheffield, United Kingdom
*Correspondence: b248967468@gmail.com

Abstract. This study investigates the crystal structures of sodium chloride and caesium chloride through powder X-ray diffraction using the Debye-Scherrer method. The primary objective was to determine lattice types, calculate lattice constants, and estimate the number of atoms per unit cell based on experimental diffraction ring data. Powdered samples were exposed to X-rays, and the resulting ring patterns were analyzed to assign Miller indices and derive interplanar spacings. The evaluation of ring positions and intensities revealed that sodium chloride crystallizes in a face-centered cubic structure, while caesium chloride adopts a body-centered cubic arrangement. The calculated lattice constants were 562.0 pm for sodium chloride and 409.6 pm for caesium chloride, both in good agreement with standard reference values. Additionally, the number of atoms per unit cell was determined to be approximately four for sodium chloride and two for caesium chloride, consistent with their respective crystal symmetries. The study confirms the reliability of basic X-ray diffraction techniques for structural identification in ionic solids and highlights distinct diffraction trends corresponding to different cubic symmetries. These findings reinforce the effectiveness of the Debye-Scherrer approach in crystallographic education and rapid phase analysis, while also identifying opportunities for enhanced resolution through extended exposure or high-intensity sources.

Keywords: X-ray diffraction, Debye-Scherrer method, crystal structure, sodium chloride, caesium chloride, lattice constant.

1. Introduction

Crystalline solids possess periodic atomic arrangements that define their physical properties and play a central role across materials science, solid-state physics, and crystallography. X-ray diffraction (XRD) is a powerful technique to probe these arrangements, and the Debye–Scherrer method, which analyzes powder samples, is particularly useful for determining structural properties such as lattice parameters and plane orientation through diffraction rings [1], [2], [3].

In cubic ionic crystals, determining whether a material adopts a face-centered cubic (fcc) or body-centered cubic (bcc) lattice is vital for understanding ionic packing density, stability, and phase behavior. Sodium chloride (NaCl) crystallizes in an fcc (rock-salt) structure, while caesium chloride (CsCl) exhibits a B2 (simple cubic with centered cation) structure often referred to as bcc-like [4], [5]. Distinguishing between these lattices using Debye–Scherrer data provides both educational and practical insights, especially when reflections overlap.

Nevertheless, contemporary challenges in Debye–Scherrer usage persist. Studies such as [6] have enhanced resolution to distinguish polymorphic alkali halides but reported ambiguities in indexing weaker peaks. [7] examined CsCl under thermal cycling, highlighting the influence of peak broadening on lattice constant determination. Automated indexing frameworks like those proposed by [8] have improved assignment reliability, yet they often fail when limited to low-angle data. Additionally, pressure-induced transitions (e.g., NaCl→CsCl phase change) underscore the method's sensitivity but also its complexity under dynamic conditions [9]. While advanced sources like

synchrotron radiation and machine-learning platforms offer high precision [10], [11], conventional laboratory Debye–Scherrer setups remain more accessible and cost-effective [12].

A significant gap remains: there's no widely adopted, stepwise, reproducible protocol for accurately identifying fcc and bcc structures from basic powder camera data and simple measurements. Past research often assumes ideal peak clarity or requires advanced tools, limiting practical application in teaching or routine materials evaluation.

We hypothesize that by systematically analyzing ring diameters, $sin^2(\theta)$ quotients, lattice constants, and unit-cell densities from Debye–Scherrer patterns of NaCl and CsCl, one can reliably distinguish fcc from bcc structures using only standard laboratory equipment.

Therefore, this study aims to:

1. Obtain diffraction data from powdered NaCl and CsCl samples using the Debye–Scherrer method.
2. Assign Miller indices, compute lattice constants, and estimate the number of atoms per unit cell.
3. Demonstrate that these analyses can reveal crystal structure reliably and reproducibly in educational or QC laboratory settings.

This work provides a clear, physically grounded workflow that reinforces crystallographic fundamentals and highlights the practical utility and limitations of simple XRD techniques.

2. Methods

2.1 Materials and Sample Preparation

Sodium chloride (NaCl, 99.5% purity, 250 g) was used as the crystalline sample for X-ray structural analysis. To prepare samples of suitable optical thickness, the NaCl was first pulverized using an agate mortar. The powdered sample was then loaded into a holder created from punched standard printer paper (2–3 layers) sealed with transparent adhesive tape to form a shallow containment cavity. This setup allowed precise control of sample thickness in the range of 0.2–0.4 mm (Figure 1).

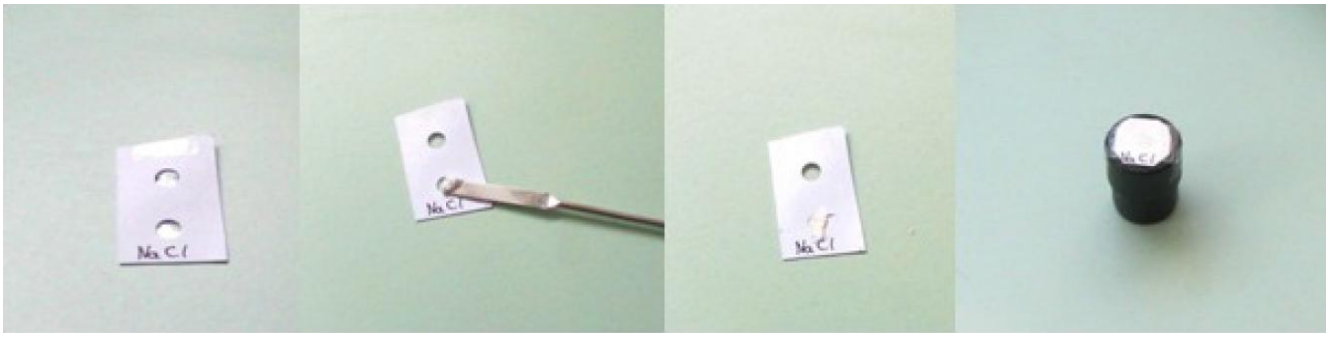

a) sample preparation b) adding the powder c) making the surface smoother d) attaching the diaphragm tube

Figure 1 – The process of NaCl samples preparation

Thickness within this range was critical to balance between sufficient edge absorption visibility and avoidance of excessive beam attenuation. Prepared samples were stored in sealed containers with silica gel to prevent moisture absorption, consistent with standard procedures for hygroscopic materials.

2.2 Experimental Setup

All measurements were performed using the XR 4.0 expert X-ray analysis system (Gulmay Ltd., UK), which included the XR 4.0 structural analysis upgrade set, XR 4.0 Plug-in Cu X-ray tube, and integrated control interface. The X-ray tube was operated at maximum capacity, with an anode voltage of 35 kV and an anode current of 1 mA, as per manufacturer guidelines.

Prior to initiating the experiment, the goniometer was removed from the internal chamber. A 1 mm-diameter diaphragm tube was installed in the beam outlet of the plug-in unit to limit the divergence of the primary beam. The X-ray-sensitive film was loaded into a light-proof film holder, which was positioned 35 mm from the NaCl crystal surface on the optical bench. The film plane was carefully aligned to remain parallel to the crystal face to ensure uniform angular resolution across the diffraction pattern. This fixed geometry was essential for consistent ring projection and accurate post-exposure evaluation.

The exposure was conducted under total darkness for a preset duration of 2.5 hours. Time tracking was performed automatically by the XR 4.0 software interface, which displayed a countdown timer and bar-graph progress. Post-exposure, the film was developed according to standard photographic chemical processing guidelines provided by the film manufacturer. The sequence included developer immersion, water rinsing, a 10-minute fixative bath, a final rewash, and air-drying.

2.3 Data Acquisition and Processing

The exposed films were analyzed using manual ring measurements, converted to diffraction angles using established geometric relationships for flat film geometry. The data acquisition was facilitated by the XR 4.0 software suite, which also recorded system parameters, exposure conditions, and environmental data (Figure 2).

a) selecting parameters b) starting a program

Figure 2 – X-Ray equipped special software

Uncertainty propagation was applied to angular measurements using standard error formulas, and regression analysis was carried out using MATLAB R2023a, applying nonlinear least squares fitting routines to extract structural parameters.

3. Results and Discussion

The structural characteristics of sodium chloride (NaCl) and caesium chloride (CsCl) were analyzed using Debye-Scherrer powder diffraction. The results are presented in the order of experimental procedures, beginning with the assignment of diffraction rings to lattice planes based on measured ring diameters and corresponding Bragg angles.

The NaCl sample (Figure 3a) displays a well-defined series of concentric rings with variable intensity. Up to seven rings are distinguishable, with higher intensities noted for the second and third reflections, consistent with the fcc (face-centered cubic) symmetry. In contrast, the CsCl pattern (Figure 3b) also reveals seven rings, albeit with a different intensity distribution. The first reflection in CsCl is significantly more intense, a feature typical of bcc (body-centered cubic) lattices where the (100) reflection is forbidden and the (110) family dominates the low-angle region.

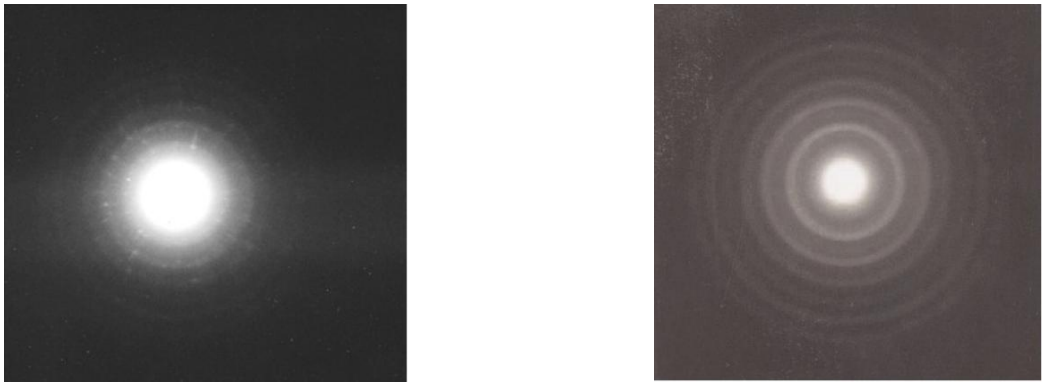

a) NaCl b) CsCl

Figure 3 – Debye-Scherrer pattern: sample thickness: 0.4 mm; exposure time: 2.5 h

The results of evaluation of the Debye-Scherrer rings of NaCl are summarized in Table 1.

Table 1 – Evaluation of the Debye-Scherrer rings of NaCl. Distance between the sample and film 32 mm + 0.5 mm film thickness. Wavelength: $\lambda(K_\alpha)$ = 71.1 pm.

No.	Intensity	D, mm	Θ, °	$\frac{\sin\theta_n}{\sin\theta_1}$	$\frac{N_n}{N_{min}}$	hkl	d, pm	a, pm
1	very weak	14.7	6.5	1.00	1.00	011	318.9	552.4
2	very strong	16.8	7.1	1.27	1.25	002	283.8	567.3
3	very strong	24.5	10.2	2.64	2.64	022	198.7	562.3
4	strong	30.6	12.7	3.84	3.82	222	163.1	564.3
5	weak	36.1	14.5	5.12	5.12	004	141.2	564.2
6	medium	42.1	16.3	6.41	6.41	024	125.9	563.1
7	weak	47.5	18.2	7.78	7.75	224	114.5	560.5

The data in Table 1 show a systematic increase in ring diameter and diffraction angle with each successive reflection. The $sin^2(\theta)$ ratios correspond well with theoretical predictions for a fcc lattice, particularly when the first reflection is indexed as the (111) plane. The Miller indices are consistent with the fcc selection rules, showing only combinations where the sum of indices is even or odd, but not mixed. The lattice constant calculated from these reflections averages a = 562.0 ± 4.7 pm, which aligns closely with the known literature value of 563.9 pm [13].

The structural analysis was then extended to CsCl using the same Debye-Scherrer method. The results are summarized in Table 2, listing the measured ring diameters, glancing angles, interplanar distances, and assigned lattice planes.

Table 2 – Evaluation of the Debye-Scherrer rings of CsCl. Distance between the sample and film: 30 mm + 0.5 mm film thickness. Wavelength: $\lambda(K_\alpha)$ = 71.1 pm.

No.	Intensity	D, mm	Θ, °	$\frac{\sin\theta_n}{\sin\theta_1}$	$\frac{N_n}{N_{min}}$	hkl	d, pm	a, pm
1	very strong	15.5	7.1	1.00	1.00	011	287.7	407.4
2	very weak	19.4	8.7	-	-	002	206.2	412.3
3	very strong	22.4	10.0	1.94	2.01	002	204.7	409.3
4	strong	27.9	12.4	2.97	3.00	112	166.8	408.6
5	weak	32.8	14.3	3.94	4.00	022	144.8	409.7
6	medium	37.9	15.8	4.92	5.00	013	129.7	410.4
7	weak	42.6	17.7	5.93	6.00	222	118.2	409.5

The progression of ring diameters and corresponding θ-values for both NaCl and CsCl displays a clear and regular increase, as expected from Bragg's Law for cubic crystal systems. In the case of NaCl, the ratios $\frac{\sin\theta_n}{\sin\theta_1}$ align well with the theoretical sequence 1:1.33:2.66:4.00:5.33:6.66:8.00, which corresponds to the allowed reflections in an fcc lattice. Notably, all observed (hkl) indices

follow the selection rule for fcc crystals: only reflections with either all even or all odd indices appear. This, combined with the calculated average lattice parameter of 562.0 ± 4.7 pm, supports the conclusion that NaCl crystallizes in the face-centered cubic structure, in agreement with the standard literature value of 563.9 pm [13], [14].

In contrast, the CsCl results exhibit a different behavior. The reflections do not adhere to the even-only or odd-only selection rules. Instead, the Miller indices include combinations such as (011), (112), and (013), which are characteristic of a bcc lattice, where allowed reflections must satisfy the condition that the sum $h+k+l$ is even. This explains the absence of the (100) reflection and the dominance of other even-summed planes. The $sin^2(\theta)$ quotient progression of 1:2:3:4:5:6 corresponds well to theoretical bcc expectations, and the mean lattice constant of 409.6±1.7pm closely matches the reference value of 411.0 pm [13], [14].

Overall, both data sets demonstrate high internal consistency and conformity with established crystallographic models. The patterns and lattice constants extracted from the Debye-Scherrer rings match not only theoretical expectations but also previously published experimental values [13], [14]. The clarity of the second and third rings in NaCl and the first in CsCl reinforces the known differences in scattering behavior and atomic packing factors between fcc and bcc structures.

4. Conclusions

The structural analysis of powdered NaCl and CsCl using Debye-Scherrer diffraction successfully confirmed their respective crystal systems: NaCl adopts a fcc lattice, while CsCl forms a bcc lattice.

For NaCl, seven diffraction rings were clearly observed, with $sin^2(\theta)$ ratios following the expected fcc pattern. The calculated average lattice constant was a = 562.0 ± 4.7 pm, consistent with the known value of 563.9 pm.

CsCl exhibited a characteristic bcc reflection pattern with even-summed Miller indices, yielding a mean lattice constant of a = 409.6 ± 1.7 pm, matching the standard 411.0 pm.

The number of atoms per unit cell was estimated as ~4 for NaCl and ~2 for CsCl, confirming their fcc and bcc identities based on density and unit cell volume calculations.

A major trend observed was the alignment of the $\sin^2(\theta)$ quotient progressions with theoretical expectations for each lattice type, validating the indexing and structure determination methodology.

The study successfully addressed the research objective by demonstrating that ring pattern analysis and basic geometric measurements can be used to identify crystal systems, calculate lattice constants, and confirm unit cell content in cubic ionic crystals.

These findings can support educational laboratory training in crystallography and may serve as a reference protocol for rapid phase identification in powder samples using basic X-ray techniques.

A constraint of the study lies in the limited exposure times, which affected the visibility of weaker high-order reflections. Future studies may incorporate synchrotron sources or longer exposures for improved resolution of marginal rings.

References

[1] K. Wang, W. Yang, X. Gao, and X. Wang, "Effect of preparation conditions on crystal size and pore structure of pseudoboehmite," Tianjin Daxue Xuebao (Ziran Kexue yu Gongcheng Jishu Ban)/Journal Tianjin Univ. Sci. Technol., vol. 46, no. 10, pp. 934–938, Oct. 2013, doi: 10.11784/TDXB20131013.

[2] K. C. Ross, J. A. Petrus, and A. M. McDonald, "An empirical assessment of two-dimensional (2D) Debye-Scherrer-type image-plate X-ray diffraction data collapsed into a 1D diffractogram," Powder Diffr., vol. 29, no. 4, pp. 337–345, Jun. 2014, doi: 10.1017/S0885715614000487.

[3] H. Yanxon et al., "Artifact identification in X-ray diffraction data using machine learning methods," J. Synchrotron Radiat., vol. 30, pp. 137–146, Jan. 2023, doi: 10.1107/S1600577522011274.

[4] S. H. Teh and I. I. Yaacob, "Synthesis and characterisation of electrodeposited iron-platinum nanostructured thin films," Mater. Res. Innov., vol. 13, no. 3, pp. 199–202, Sep. 2009, doi: 10.1179/143307509X437617.

[5] Y. Teshima and T. Matsumoto, “Continuous deformation of sphere-packing structures extending over simple, body-centered, and face-centered cubic lattices,” Glas. Phys. Chem., vol. 38, no. 1, pp. 49–54, Feb. 2012, doi: 10.1134/S1087659612010154.
[6] S. V. Karpenko, A. P. Savintsev, and A. I. Temrokov, “Anomalous behavior of surface characteristics of certain ionic crystals under high pressures,” Dokl. Phys., vol. 53, no. 3, pp. 128–132, 2008, doi: 10.1134/S102833580803004X.
[7] X. Wang et al., “Revisiting lattice thermal conductivity of CsCl: The crucial role of quartic anharmonicity,” Appl. Phys. Lett., vol. 124, no. 17, Apr. 2024, doi: 10.1063/5.0201393.
[8] H. Ling, J. Montoya, L. Hung, and M. Aykol, “Solving inorganic crystal structures from X-ray powder diffraction using a generative first-principles framework,” Comput. Mater. Sci., vol. 214, p. 111687, Nov. 2022, doi: 10.1016/J.COMMATSCI.2022.111687.
[9] P. Tolédano, K. Knorr, L. Ehm, and W. Depmeier, “Phenomenological theory of the reconstructive phase transition between the NaCl and CsCl structure types,” Phys. Rev. B - Condens. Matter Mater. Phys., vol. 67, no. 14, Apr. 2003, doi: 10.1103/PHYSREVB.67.144106.
[10] Y. Liu et al., “Progress and challenges in structural, in situ and operando characterization of single-atom catalysts by X-ray based synchrotron radiation techniques,” Chem. Soc. Rev., Oct. 2024, doi: 10.1039/D3CS00967J.
[11] J. Santana-Andreo, H. D. Saßnick, and C. Cocchi, “Thermodynamic stability and vibrational properties of multi-alkali antimonides,” JPhys Mater., vol. 7, no. 3, Jul. 2024, doi: 10.1088/2515-7639/AD510B.
[12] F. Logiurato, L. M. Gratton, and S. Oss, “Optical Simulation of Debye-Scherrer Crystal Diffraction,” Phys. Teach., vol. 46, no. 2, pp. 109–112, Feb. 2008, doi: 10.1119/1.2834534.
[13] “Introduction to Solid State Physics Charles Kittel,” 2005.
[14] D. W. Snoke, “Solid State Physics: Essential Concepts,” Jan. 2020, doi: 10.1017/9781108123815.

Information about authors:
Marry Brewer – PhD, Research Assistant, Department of Materials Science, Sheffield Hallam University, Sheffield, United Kingdom, b248967468@gmail.com

Author Contributions:
Marry Brewer – concept, methodology, resources, data collection, testing, modeling, analysis, visualization, interpretation, drafting, editing, funding acquisition.

Conflict of Interest: The authors declare no conflict of interest.

Use of Artificial Intelligence (AI): The authors declare that AI was not used.

Received: 11.05.2025
Revised: 03.06.2025
Accepted: 07.06.2025
Published: 11.06.2025

Technobius Physics, 2025, 3(2), 0032, DOI: https://doi.org/10.54355/tbusphys/3.2.2025.0032

Technobius Physics

https://technobiusphysics.kz/

e-ISSN 3007-0147

Post-Publication Notice

Retraction to "M. Brewer and A. Sheriyev, "Structural analysis of NaCl and CsCl via Debye–Scherrer powder diffraction", tbusphys, vol. 3, no. 2, p. 0031, Jun. 2025. doi: 10.54355/tbusphys/3.2.2025.0031"

Following the publication of the article, the Editorial Board received an official complaint from Mr. Almas Sheriyev on 18 June 2025, stating that his name was listed as a co-author without his knowledge or consent. Per the journal's Publication Ethics, we contacted the corresponding author the same day and requested a formal clarification. On 23 June 2025, we received the response from the corresponding author, who gave her full consent to proceed with the retraction.

Given the serious nature of this authorship violation and consent from the corresponding author to proceed with the retraction, the Editorial Board has decided the following:

- To retract the article.
- To correct the originally published version by removing Mr. Almas Sheriyev from the list of authors and removing the information about him from the article.
- To publish the current retraction notice in the Post-Publication Notice section of the journal's current issue.
- To inform indexing services of both the retracted and the corrected article.

The Editorial Board regrets that this authorship violation occurred and sincerely apologizes to Mr. Almas Sheriyev and our readers for any confusion or inconvenience caused.

Published: 23.06.2025

Technobius Physics, 2025, 3(1), 0033, DOI: https://doi.org/10.54355/tbusphys/3.2.2025.0033

Technobius Physics

https://technobiusphysics.kz/

e-ISSN 3007-0147

Article

Advanced characterization of atomic terraces and electronic topography of graphite using STM in constant current and constant height modes

Medet Mustafin*

Department of Physics and Technology, Al-Farabi Kazakh National University, 71 Al-Farabi ave., Almaty, Kazakhstan
*Correspondence: medet.mustafin.01@mail.ru

Abstract. This study presents a high-resolution scanning tunneling microscopy analysis of highly ordered pyrolytic graphite, aimed at quantitatively characterizing atomic-scale surface features using both constant-current and constant-height imaging modes. Building upon previous work, the investigation focuses on step height measurements and lattice parameter evaluation across multiple scan areas. STM images captured in constant-current mode revealed clear atomic terraces and hexagonal lattice patterns, with step heights measured at approximately 332.2–333.9 pm, closely matching the theoretical monolayer thickness of graphite. Interatomic distances between nearest neighbors (~140 pm) and atomic rows (~245–248 pm) were also consistent with known lattice parameters. In constant-height mode, tunneling current profiles were recorded along line scans of 1.25 nm and 20.7 nm. These profiles exhibited periodic current modulations corresponding to atomic corrugation, with amplitude variations of approximately 0.2 nA. The data confirm the STM's capacity to resolve both vertical and lateral atomic features with high precision. The study demonstrates the effectiveness of combining imaging modes to extract complementary structural and electronic information from layered crystalline surfaces. The results contribute a validated reference framework for STM calibration and underscore the technique's reliability in distinguishing atomic-scale topography and local electronic contrast.
Keywords: scanning tunneling microscopy, graphite, atomic terraces, constant height mode, tunneling current, LDOS.

1. Introduction

The ability to visualize and quantify atomic-scale features on solid surfaces plays a critical role in advancing nanotechnology, materials science, and surface physics. Scanning tunneling microscopy (STM) remains one of the most powerful tools for achieving atomic-resolution imaging of conductive and semiconductive surfaces [1]. It enables not only topographic visualization but also the investigation of local electronic properties via measurement of the tunneling current, which is exponentially dependent on the tip–sample separation and the local density of states. One particularly well-studied material for STM calibration and benchmarking is highly ordered pyrolytic graphite (HOPG), whose layered hexagonal lattice provides an ideal test system for atomic-resolution analysis [2].

Despite decades of research, challenges persist in accurately measuring atomic step heights and interatomic distances, particularly when comparing results from different STM operation modes—namely, constant-current and constant-height imaging [3], [4]. Constant-current mode, while widely used for topographic imaging, introduces convolution between electronic and geometric effects. Constant-height mode, in contrast, offers enhanced sensitivity to local variations in electronic structure but demands a highly stable system and precise control. Bridging these imaging approaches to extract robust, quantitative metrics of surface morphology and electronic contrast remains an ongoing challenge.

Recent original research has attempted to address these limitations. For example, [5] employed high-resolution STM to characterize step edge formation on HOPG during controlled etching, reporting variations in measured step heights due to tip convolution effects. Similarly, [6] demonstrated that even with atomically flat terraces, discrepancies between apparent and actual height values persist due to local density of states modulation. Furthermore, in a comparative study, [7] analyzed STM profiles in both modes and concluded that while constant-height mode yields more precise electronic contrast, it is susceptible to mechanical instabilities. These studies underscore the need for systematic, side-by-side analysis of atomic step heights and lattice periodicities using both imaging techniques on well-defined samples.

However, the literature still lacks a detailed methodological comparison using the same sample area imaged in both constant-current and constant-height modes to directly quantify the topographic and electronic contrast resolution. Moreover, most studies focus on isolated aspects—either step heights or atomic contrast—without integrating these into a single comprehensive data set. This represents a gap in the field, especially in the context of instrument calibration, measurement reproducibility, and the interpretation of electronic structure in layered materials like graphite.

We hypothesize that a combined STM analysis of HOPG in both constant-current and constant-height modes on the same scan regions can provide complementary insight into atomic-scale surface topography and electronic variation, offering a higher confidence level in step height measurements and lattice parameter resolution. We further assume that quantitative current profiling in constant-height mode can capture subtle differences in the local density of states that are averaged out in traditional constant-current imaging.

The goal of this study is to extend previous work by performing a comprehensive STM-based analysis of HOPG surfaces at multiple scales, combining high-resolution imaging, atomic step height measurement, and tunneling current profiling in both constant-current and constant-height modes. This approach not only confirms the calibration accuracy of the STM system but also demonstrates the method's capacity to distinguish topographic and electronic features with atomic precision. The novelty of this study lies in its integrative methodology and its application to a model system with known crystallography, thereby contributing a validated reference framework for future STM-based materials characterization.

2. Methods

2.1 Study Design and Continuity

This study is a continuation of our previous work on the application of STM for imaging molecular assemblies on graphite and functionalized surfaces [8]. In this extended study, we focused on high-resolution imaging of atomic terraces and interatomic distances on HOPG surfaces using both constant-current and constant-height STM modes.

2.2 Materials and Sample Preparation

Highly oriented pyrolytic graphite (HOPG) was used due to its atomically smooth, layered crystalline structure. To prepare clean surfaces, samples were cleaved using adhesive tape. STM tips were fabricated from platinum–iridium (Pt–Ir) wire using mechanical fracture at a sharp angle, producing a nanometer-sharp apex optimal for tunneling current detection.

2.3 Instrumentation and Measurement Conditions

Scanning tunneling microscopy was performed using a Nanosurf NaioSTM system (Nanosurf AG, Switzerland), featuring active vibration isolation and closed-loop piezoelectric positioning in x, y, and z directions with sub-nanometer resolution. Measurements were conducted in ambient air.

The microscope operated in both constant-current and constant-height modes. Key parameters used throughout the study were bias voltage of 1.2 V; setpoint tunneling current of 1.2 nA; PID feedback are P-gain = 1200, I-gain = 1500; scan time per line is 0.03 s.; resolution: 128 points per line.

For constant-height imaging, the z-feedback was disabled after tip stabilization, and tip–sample distance was adjusted via the relative tip position from –25 nm to –0.14 nm.

2.4 Data Acquisition and Processing

Image acquisition was performed using Nanosurf EasyScan 2 software. Image processing and topographical analysis were conducted using Gwyddion 2.63, which enabled plane correction, noise filtering, and extraction of line profiles for terrace height and interatomic spacing measurements.

2.5 Measurement Protocol and Statistical Treatment

To capture atomic features, scan areas were reduced from 30 nm to 10 nm, and finally to 3 nm. Structural data, such as terrace step heights and atomic row spacing, were derived from multiple line profiles. Each type of measurement was repeated three to five times to ensure reproducibility. The mean and standard deviation were reported. Values were compared to known crystallographic standards (e.g., graphene layer thickness ≈ 334.8 pm) for validation.

Measurement errors can be caused by the scanning process itself, in particular due to the temperature dependence of the piezoelectric device. However, more significant deviations are often associated with improper *z* alignment along the z-axis or incorrect background correction. To ensure consistency and accuracy, the relative deviation from the literature values should not exceed approximately 2%; ideally, this error should be minimised even further. Upon completion of the measurements, the average value of the data corresponding to each specified step size was calculated to increase the reliability of the results using the formula:

$$\overline{m} = \frac{1}{N}\sum_{j=1}^{N} v_j \quad (1)$$

Where, every v_j value had divided the sum by the number of values. The standard deviation was another statistical measure that had indicated the accuracy of the measurements:

$$s = \frac{1}{N-1}\sum_{j=1}^{N} j - \overline{m^2} \quad (2)$$

3. Results and Discussion

3.1 Atomic-Scale Imaging and Step Height Measurement

Figure 1 presents topographic STM images of HOPG at progressively reduced scan areas of 30 nm, 10 nm, and 3 nm. These images were captured in constant-current mode to visualize atomic terrace steps and atomic lattices.

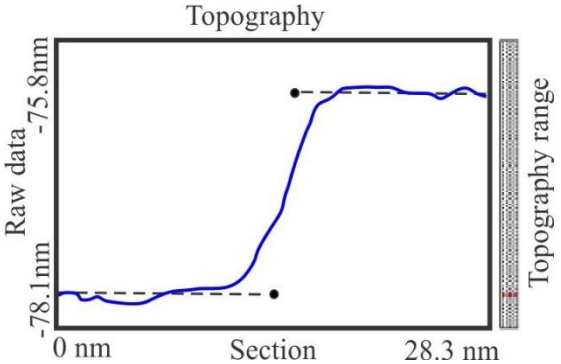

Figure 1 – Cross section of atomic terraces at distance of Δz = 332.2 pm

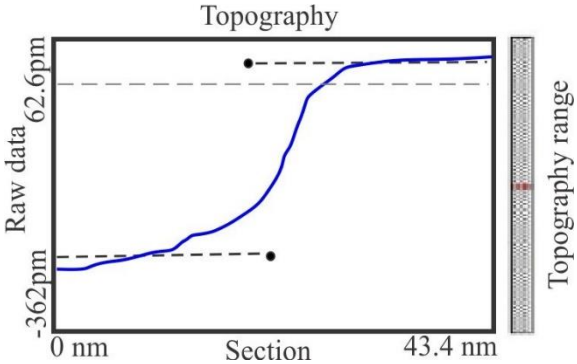

Figure 2 – Cross section of atomic terraces at distance of Δz = 332.9 pm

In Figure 1, larger terrace features are visible, whereas at 10 nm and 3 nm, atomic resolution is achieved, revealing the characteristic hexagonal pattern of the graphite surface. In Figure 2 cross-sectional profiles drawn across these images show measured step heights of 332.2 pm and 333.9 pm (±1.2 pm), in close agreement with the theoretical monolayer thickness of graphite (334.8 pm).

This confirms the STM's capacity to resolve single-layer steps. The interatomic spacing observed between rows and nearest neighbors (245–248 pm and ~140 pm, respectively) matches the known graphite lattice constants, validating the calibration and imaging precision.

3.2 Constant-Height Mode and Tunneling Current Profiles

As previous work has shown [8], every second atom has a neighbouring atom in the lower layer. Each atom in the upper layer loses electron density to its nearest neighbour in the lower layer, causing these atoms to appear darker in images obtained using STM. In contrast, atoms that do not have a direct neighbour below retain their full electron density and appear as bright spots. As noted earlier [8], it was useful to take measurements using linear scans rather than simple point-to-point measurements, as this approach allowed for more accurate determination of the distance between atoms. This trend also confirms trends in Figure 3. In this work, the desired structural information was also obtained using cross-sections. By drawing a line through a series of atoms and measuring the distance on the resulting graph, it was possible to choose whether to measure the distance from one atom to another (from peak to valley, with an approximate distance (d=140 pm) or from one row of atoms to another (from peak to peak or from valley to valley, with an approximate distance (d=245 pm; Figure 4).

In order to increase the accuracy of measurements and minimise systematic errors, the distance between 5–10 rows of atoms was measured and then divided by the number of rows, which gave the average distance between rows. Figure 2 shows STM results obtained in constant-height mode with the z-feedback loop disabled. Tip–sample distance was controlled by modifying the relative tip position.

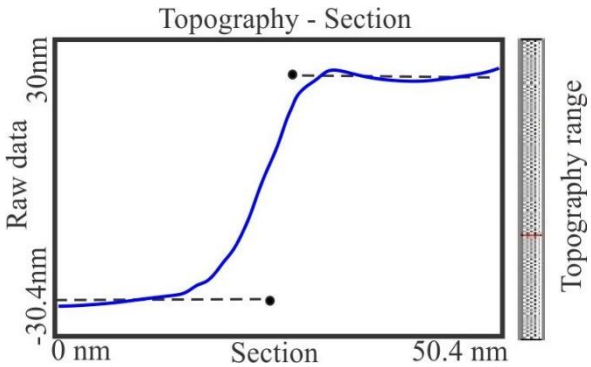

Figure 3 – Cross section of atomic terraces at distance of Δz = 686.1 pm

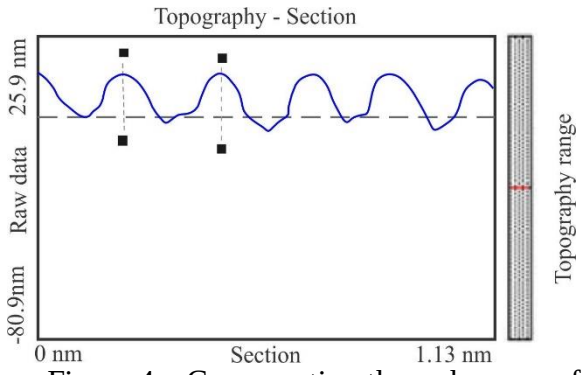

Figure 4 – Cross section through a row of atoms. Distance between lines: d=248.5 pm (hill to hill) z=15.3pm (hill-top to valley)

All images acquired thus far have been obtained using the constant current mode, in which the tunneling current between the tip and the sample has been maintained at a constant value. Since the tip–sample distance is proportional to the tunneling current, this distance has also remained effectively constant. In this mode, the measurement signal has been the elongation of the z-piezo element, which controls the vertical movement of the tip and closely follows the surface topography. We now consider the constant height mode, an advanced scanning technique in which the height of the tip above the sample surface is fixed at a predetermined value.

Figure 5 presents the STM graph presented, obtained in constant height mode, shows the tunnel current profile along a line 20.7 nm long. In the initial section (0–6 nm), the signal remains stable (~337 pA), which corresponds to a relatively flat surface. Further on, a sharp increase in current (up to ~1 nA) is observed in the 6–10 nm section, indicating the presence of a step or a sharp change in the density of states. In the 10–18 nm range, the curve stabilizes with minor fluctuations, reflecting a more homogeneous upper region. At the end of the profile (18–20.7 nm), a small increase in the signal is recorded, possibly associated with local features of the relief or electronic structure. This type of current distribution indicates the presence of terraces and atomic steps on the surface of the sample under study.

Figure 6 shows the profile of the tunneling signal along a line 1.25 nm long, taken from the surface of graphite with atomic resolution.

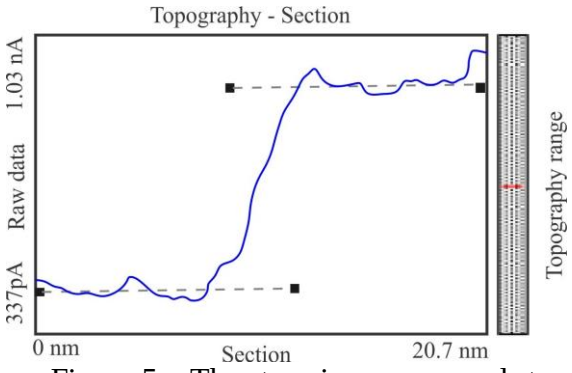

Figure 5 – The step size corresponds to a difference in the tunneling current of 578.6 pA (or 334.8 pm, one atomic layer)

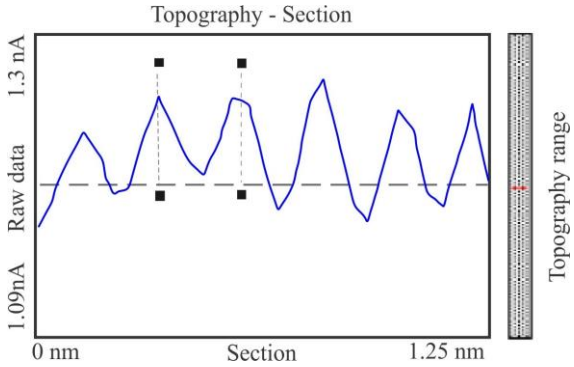

Figure 6 – Cross sectioning: Distance between lines: d=235.1 pm (hill to hill, hill to val-ley gives: d=117.4 pm. The zdistance from hilltop to valley corresponds to the measured current: I=81.68 pA

The amplitude of the tunneling current varies between 1.09 and 1.3 nA, which corresponds to the relief formed by individual carbon atoms. The graph clearly shows periodic signal modulation with a step of about 0.246 nm, which coincides with the interatomic distance in the hexagonal graphene lattice. A total of about five maxima corresponding to five atomic columns are visualized on the profile. The vertical dotted lines and black square markers indicate the boundaries of one characteristic oscillation period, which can be used to estimate the height amplitude of the signal (~0.2 nA). On the right is a scale of the section position on a two-dimensional topographic map of the sample. Such a distribution of the tunnel current indicates high structural regularity and planar uniformity of the graphite surface, and also confirms the reliability of the STM at the atomic scale.

4. Conclusions

1. STM imaging of HOPG revealed atomic terraces and step heights of 332.2–333.9 pm, closely matching the theoretical monolayer thickness of 334.8 pm.

2. Atomic-resolution scans showed interatomic distances of ~140 pm between nearest neighbors and ~245–248 pm between atomic rows, consistent with graphite's lattice parameters.

3. Constant-height mode enabled detailed tunneling current profiling, revealing periodic modulations with amplitudes of ~0.2 nA and step sizes corresponding to one atomic layer.

4. The study confirms STM's capability to resolve both vertical and lateral atomic-scale features with high precision.

5. These findings address the research goal of validating STM performance in resolving graphite's atomic structure.

6. Results can be applied for surface quality assessment and calibration of STM systems.

7. Limitations include reliance on ideal graphite samples; future work may explore defect structures and other materials.

References

[1] S. Yngman et al., "GaN nanowires as probes for high resolution atomic force and scanning tunneling microscopy," Rev. Sci. Instrum., vol. 90, no. 10, Oct. 2019, doi: 10.1063/1.5122791.

[2] D. A. C. Brownson, R. V. Gorbachev, S. J. Haigh, and C. E. Banks, "CVD graphene vs. highly ordered pyrolytic graphite for use in electroanalytical sensing," Analyst, vol. 137, no. 4, pp. 833–839, Feb. 2012, doi: 10.1039/C2AN16049H.

[3] A. C. Campbell, P. Jelínek, and P. Klapetek, "Study of uncertainties of height measurements of monoatomic steps on Si 5 × 5 using DFT," Meas. Sci. Technol., vol. 28, no. 3, Jan. 2017, doi: 10.1088/1361-6501/AA5075.

[4] E. V. Sysoev and A. V. Latyshev, "Measuring the Interatomic Distance in a Silicon Crystal Lattice Using an Optical Scanning Interferometer," Optoelectron. Instrum. Data Process., vol. 57, no. 6, pp. 561–568, Dec. 2021, doi: 10.3103/S8756699021060157.

[5] M. Zhao et al., "Insight into STM image contrast of n-tetradecane and n-hexadecane molecules on highly oriented pyrolytic graphite," Appl. Surf. Sci., vol. 257, no. 8, pp. 3243–3247, Feb. 2011, doi: 10.1016/j.apsusc.2010.10.150.
[6] T. Carstens et al., "Combined STM, AFM, and DFT study of the highly ordered pyrolytic graphite/1-octyl-3-methyl-imidazolium bis(trifluoromethylsulfonyl)imide interface," J. Phys. Chem. C, vol. 118, no. 20, pp. 10833–10843, May 2014, doi: 10.1021/JP501260T.
[7] H. Ma et al., "Scanning tunneling and atomic force microscopy evidence for covalent and noncovalent interactions between aryl films and highly ordered pyrolytic graphite," J. Phys. Chem. C, vol. 118, no. 11, pp. 5820–5826, Mar. 2014, doi: 10.1021/JP411826S.
[8] M. Mustafin, "Probing molecular architectures and interactions with scanning tunneling microscopy on graphite and arachidic acid functionalized surfaces," Technobius Phys., vol. 2, no. 2, pp. 0010–0010, Apr. 2024, doi: 10.54355/TBUSPHYS/2.2.2024.0010.

Information about authors:
Medet Mustafin – Master Student, Department of Physics and Technology, Al-Farabi Kazakh National University, 71 Al-Farabi ave., Almaty, Kazakhstan, medet.mustafin.01@mail.ru

Author Contribution:
Medet Mustafin – concept, methodology, resources, data collection, testing, modeling, analysis, visualization, interpretation, drafting, editing, funding acquisition.

Conflict of Interest: The authors declare no conflict of interest.

Use of Artificial Intelligence (AI): The authors declare that AI was not used.

Received: *12.05.2025*
Revised: 20.06.2025
Accepted: 26.06.2025
Published: 29.06.2025

Technobius Physics, 2025, 3(2), 0034, DOI: https://doi.org/10.54355/tbusphys/3.2.2025.0034

Technobius Physics

https://technobiusphysics.kz/

e-ISSN 3007-0147

Article

Confocal and time-resolved photoluminescence spectra of $MgAl_2O_4$ spinel crystals irradiated with swift heavy bismuth ions

Abdrash Akilbekov[1], Nikita Kirilkin[2], Meruert Mamatova[1,2,*]

[1]Deparmnet of Physics, L N Gumilyov Eurasian national University, Astana, Kazakhstan
[2]Joint Institute for Nuclear Research, Dubna, Russian Federation
*Correspondence: meruert.mamatova@mail.ru

Abstract. Laser confocal microscopy technique (60 ps laser pulse excitation at 445 nm) and a time-correlated single photon counting (TCSPC) technique have been used to study photoluminescence (PL) in 710 MeV Bi ion irradiated MgAl2O4 single crystals. It was shown that radiation defects produced by swift Bi ions give rise to luminescence with peak at 1.9 eV. Gaussian deconvolution of the PL spectrum reveals that the band consists of three components: the first with a peak at 1.8 eV, the second at 2.1 eV, and the third at 2.35 eV. For the spinel sample irradiated to a fluence of $\Phi = 1\times10^{12}$ ions/cm², both PL and time-resolved photoluminescence (TRPL) spectra were measured as a function of depth within the irradiated layer using a confocal geometry. It was found that with increasing energy loss due to elastic collisions, the PL peak undergoes a redshift, which is more pronounced compared to surface emission measurements.
Keywords: MgAl2O4 single crystals, confocal and time-resolved photoluminescence, radiation-induced defects, swift heavy ions, tracks.

1. Introduction

Aluminum-magnesium spinel, $MgAl_2O_4$, is one of the most extensively studied optical materials due to its high radiation resistance, chemical and thermal stability, mechanical strength, and optical transparency across a wide spectral range—from infrared to ultraviolet. These properties make it suitable for use as an inert matrix for the transmutation of long-lived actinides, diagnostic windows in fusion reactors, and in dosimetry applications when doped with transition 3d elements or rare-earth ions to achieve desired optical properties, among other uses [1], [2], [3].

This potential for various applications has driven continuous and extensive research into the structure and optical properties of spinel using various radiation sources, primarily neutron and low-energy ion irradiation [3], [4], [5], [6], [7]. Notably, it has been found that $MgAl_2O_4$ does not amorphize under irradiation at temperatures above 300 K up to a radiation damage dose of approximately 100 dpa [7]. At the same time, spinel—with a relatively low threshold for specific ionization energy loss (~7.5 keV/nm) required to form latent tracks—is sensitive to swift heavy ion irradiation that simulates the impact of fission fragments [8].

A detailed analysis of ion track morphology in spinel was carried out in [9], [10][13-16], where the configuration of isolated ion tracks induced by 200 MeV Xe and 350 MeV Au ions in stoichiometric spinel, $MgO{\cdot}Al_2O_3$, was studied using high resolution transmission electron microscopy with bright-field imaging (HR-TEM) combined with high-angle resolution X-ray spectrometry. It was shown that a single ion track in spinel appears as a circle consisting of three concentric defect zones. At the center, a phase transformation to a NaCl-type rock-salt structure was observed (1 nm in radius). This rock-salt-like defect structure was surrounded by a strained region (radius of 3 nm) and a cation-disordered zone (approximately 5–6 nm in radius). Multiple overlapping

non-amorphous discontinuous ion tracks led to full amorphization of the irradiated layer in $MgAl_2O_4$ [11].

X-ray diffraction analysis [10] revealed an order-disorder transition in $MgAl_2O_4$ irradiated with 765 MeV Kr ions at a high fluence of 10^{14} cm^{-2} and partial amorphization, without any change in the space group. However, there was no evidence of a phase transformation to a rock-salt structure, as the electronic stopping power of 765 MeV Kr ions (Se ~ 14 keV/nm) is significantly lower than that of 350 MeV Au ions (Se ~ 35 keV/nm).

As far as we know, photoluminescence of $MgAl_2O_4$ irradiated with high-energy heavy ions in the regime where electronic stopping exceeds the track formation threshold has not been reported.

The present paper deals with the photoluminescence and pulsed photoluminescence of spinel crystals irradiated with 710 MeV bismuth when tracks are also created.

2. Methods

In this study, single crystals of stoichiometric $MgAl_2O_4$ spinel with a thickness of 500 μm and (100) orientation, purchased from CRYSTAL GmbH (grown using the Czochralski method), were used. The samples were irradiated with 710 MeV Bi ions at fluences ranging from 1×10^{10} to 2×10^{12} cm^{-2} at room temperature using the IC-100 cyclotron at FLNR, JINR, Dubna. The homogeneity of the ion beam across the irradiated sample surface was monitored via horizontal and vertical beam scanning and was better than 10%.

To exclude the influence of the unirradiated part of the crystal and to detect the stimulated emission solely from the near-surface layer of the sample, we employed laser confocal microscopy. As is well known, unlike standard photoluminescence measurement geometries, confocal microscopy provides spatial localization of the excitation light beam and enables luminescence detection with a spatial resolution of approximately 1 μm. In our case, this allows measurements to be conducted within the target layer, where structural modifications are predominantly driven by ionization energy loss.

Photoluminescence (PL) spectra and kinetics were measured using an Ntegra Spectra confocal scanning microscope (NT-MDT). The luminescence was excited by a picosecond laser diode head (PDL 800-D, PicoQuant) operating at an excitation wavelength of 445 ± 3 nm and a pulse duration of approximately 60 ps. The spectra were collected from a subsurface layer no thicker than 2 μm. The optical system provided a depth resolution of 1.7 μm, as determined by scanning the laser spot across the crystal edge and calculating the first derivative of the luminescence intensity. The decay of time-resolved photoluminescence (TRPL) at selected wavelengths within the 500–650 nm spectral range was measured using the time-correlated single photon counting (a time-correlated single photon counting (TCSPC) technique) technique. Decay curves were analyzed using Easytag 2 software [9]. The signal from the photomultiplier tube (PMA 175, PicoQuant), along with the synchronization signal from the diode laser, served as inputs for the TCSPC board (TimeHarp, PicoQuant). The temporal resolution of the system was approximately 200 ps.

3. Results and Discussion

Luminescence was excited at a wavelength of 445 nm (2.75 eV) using pulses with a full width at half maximum (FWHM) of less than 80 ps. Decay curves in the spectral range of 500–700 nm were recorded using a system based on a PMA-175 detector and a TCSPC module, with a temporal resolution of 300 ps. Figure 1 shows the PL dependence on fluence under irradiation with 710 MeV Bi ions, measured in a standard geometry. A broad PL band is observed in the range of 450–750 nm (2.76–1.6 eV). As the fluence increases, the luminescence intensity also increases. A slight redshift of the emission peak is observed. Figure 2 presents the Gaussian decomposition of the PL spectrum at a fluence of 2×10^{12} ions/cm^2. It consists of three bands: the first with a peak at 1.8 eV and FWHM

of 0.3 eV; the second with a peak at 2.1 eV and FWHM of 0.4 eV; and the third with a peak at 2.35 eV and FWHM of 0.23 eV.

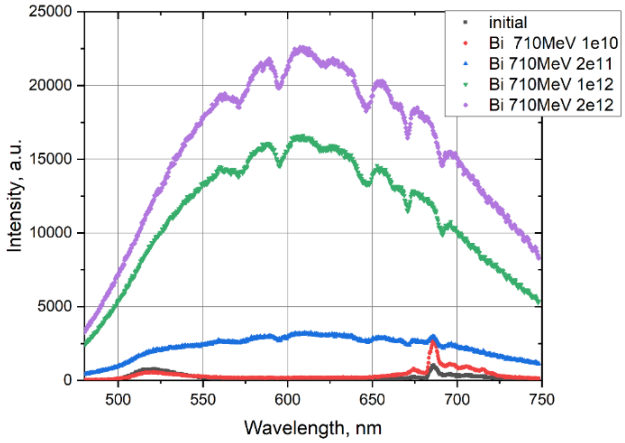

Figure 1 – Photoluminescence spectra of $MgAl_2O_4$ crystals irradiated with 710 MeV Bi ions under excitation at λ_{ex} = 445 nm

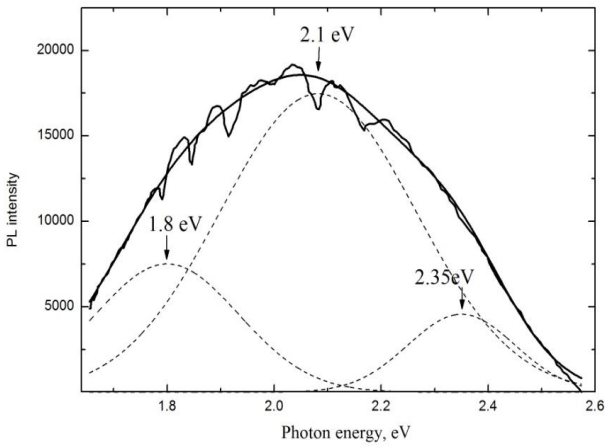

Figure 2 – Gaussian decomposition of the photoluminescence spectrum of $MgAl_2O_4$ crystals irradiated with 710 MeV Bi ions under excitation at λex = 445 nm

For the $MgAl_2O_4$ spinel sample irradiated to a fluence of $\Phi = 1\times10^{12}$ cm^{-2}, depth-resolved PL and TRPL spectra were measured using confocal geometry. Figure 3 shows PL spectra recorded on a cross-sectional cleavage at depths of 2, 12, and 24 μm from the irradiated surface. It was found that, with increasing energy loss due to elastic collisions, the PL peak shifts toward longer wavelengths. This redshift is more pronounced than in surface emission measurements, indicating that it is caused by defects generated via nuclear energy loss mechanisms.

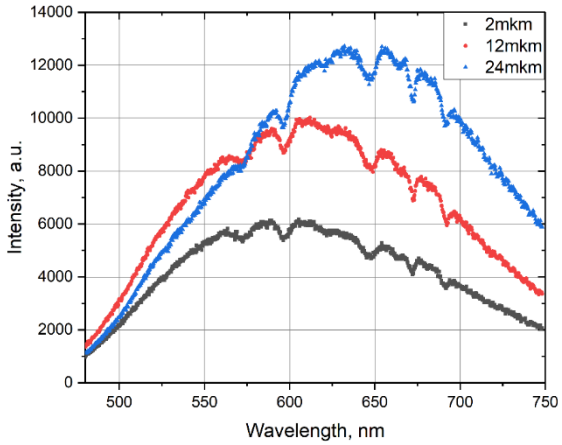

Figure 3 – Depth dependence of the photoluminescence spectra of an $MgAl_2O_4$ single crystal irradiated with Bi ions to a fluence of 1×10^{12} cm^{-2}. Excitation wavelength: λex = 445 nm

A similar effect was previously observed in LiF crystals [18], where enhanced PL from F_2 and F_3^+ aggregate color centers was detected. It was suggested that, at the end of the ion track—where elastic collisions dominate—vacancy production contributes significantly. In $MgAl_2O_4$, intrinsic luminescent centers include F^+ and F centers, antisite defects, and exciton-related emission. According to [12], at high concentrations of F^+ and F centers, PL with a peak at 2.7 eV is observed, attributed to radiative transitions from excited to ground states of F^+ and F centers. This 2.7 eV emission is predominantly excited through absorption by F^+ centers, likely surrounded by a high density of defects within their first and second coordination shells.

X-ray excitation of $MgAl_2O_4$ crystals results in a broad emission band in the spectral range of 3.15–4.2 eV (295–354 nm), which, according to [12], is attributed to antisite defects (AD). The origin of PL with a maximum at 5.3 eV remains unclear [13]. The most common impurities in the $MgAl_2O_4$ matrix are Cr^{3+} and Mn^{2+} ions [13], as confirmed by the photoluminescence of the as-grown, unirradiated $MgAl_2O_4$ crystals shown in Figure 4.

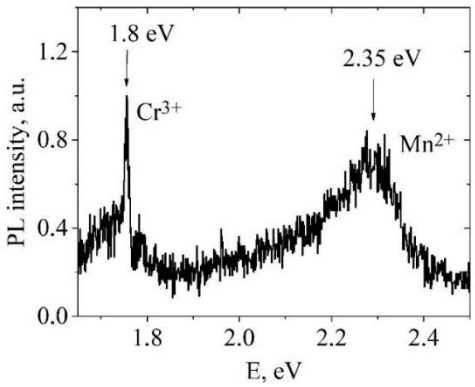

Figure 4 – Photoluminescence spectrum of an unirradiated $MgAl_2O_4$ crystal excited at 2.78 eV (445 nm)

A sharp shift of the maximum from 2.1 eV at a distance of 12 μm to 1.9 eV at the end of the ion path, accompanied by a surge in intensity, indicates that the stopped bismuth ion created a deformation field around itself. The track region is amorphized.

Figure 5 shows the kinetic decay curves measured at the same points as the PL spectra (Figure 4). The measurements were taken at the maximum of the PL band. The lifetimes of the excited states were determined.

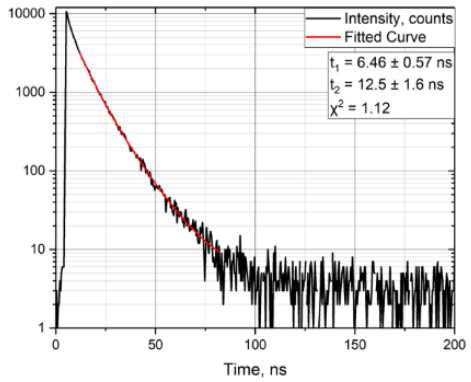

a) Data measured at depths of 2 μm

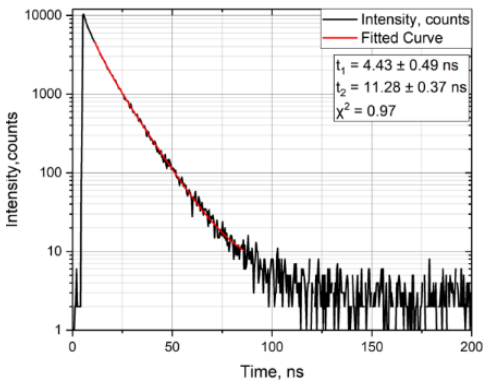

b) Data measured at depths of 12 μm

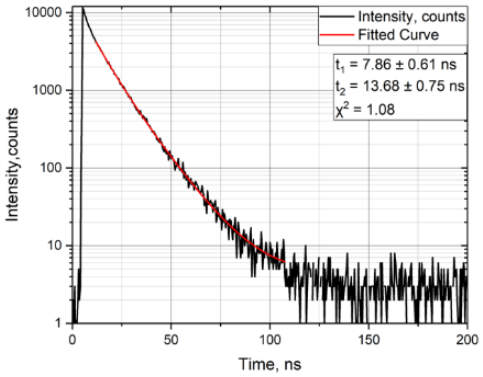

c) Data measured at depths of 24 μm

Figure 5 – Photoluminescence decay kinetics of an $MgAl_2O_4$ single crystal irradiated with Bi ions to a fluence of 1×10^{12} cm^{-2}

A distinguishing feature of the PPL band at 1.9–2.1 eV is its strong intensity at room temperature. The decay kinetics of the 1.9 eV band at T = 296 K can be described by a double-exponential function with two distinct characteristic lifetimes, as presented in Table 1. Based on the data in Table 1, it can be concluded that the characteristic decay times of both the fast and slower components of the PPL signal are independent of depth within the measurement uncertainty.

Table 1 – Example of a table

Depth, μ m	t_1, ns	t_2, ns
2	6.46±0.57	12.5 ±1.6
12	4.43±0.49	11.28±0.37
24	7.86±0.61	13.68±0.75

The formation of tracks in $MgAl_2O_4$ spinel crystals irradiated with 710 MeV ions is beyond doubt, as track formation has been previously observed under irradiation with 100 MeV Xe, 200 MeV Xe, and 340 MeV Au ions [8], [14], [15]. For instance, the track diameter for 100 MeV Xe ions is reported to be 4.9–5.1 nm based on small-angle X-ray scattering data [15], which agrees well with the size of the deformed region observed via transmission electron microscopy [2].

Figure 6 shows transmission electron microscopy images of radiation-induced microstructural changes in spinel crystals irradiated with Bi ions to a fluence of 10^{11} cm^{-2}, obtained at the Joint Institute for Nuclear Research (JINR), Dubna.

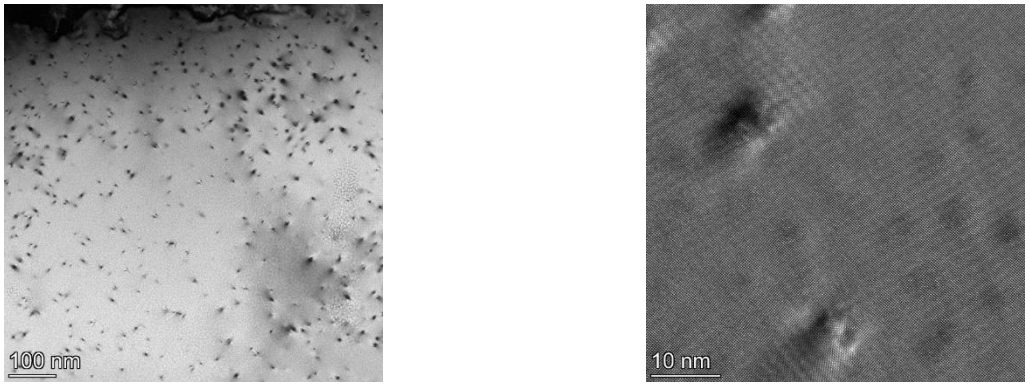

a) Data measured at 100 nm b) Data measured at 10 nm

Figure 6 – High-resolution transmission electron microscopy images of latent ion tracks in $MgAl_2O_4$ spinel irradiated with Bi ions

The track diameter for 100 MeV Xe ions, for example, is reported to be 4.9–5.1 nm based on small-angle X-ray scattering data [26], which coincides with the size of the deformed region observed by transmission electron microscopy [13, 23].

The observed photoluminescence is highly sensitive to structural disorder and is likely associated with the emission from aggregate electronic color centers, such as F_2^{2+} centers in Al_2O_3, which exhibit a luminescence peak at 2.2 eV [27]. These centers typically form at high fluences due to track overlapping. The 1.9 eV luminescence enhancement near the end of the ion trajectory may be related to the creation of vacancies.

4. Conclusions

A photoluminescence (PL) band at 1.9 eV is observed in $MgAl_2O_4$ spinel irradiated with 710 MeV Bi ions. Gaussian deconvolution of the PL spectrum reveals that the band consists of three components: the first with a peak at 1.8 eV and a full width at half maximum (FWHM) of 0.3 eV, the second at 2.1 eV (FWHM = 0.4 eV), and the third at 2.35 eV (FWHM = 0.23 eV).

For the spinel sample irradiated to a fluence of $\Phi = 1\times10^{12}$ ions/cm², both PL and time-resolved photoluminescence (TRPL) spectra were measured as a function of depth within the

irradiated layer using a confocal geometry. It was found that with increasing energy loss due to elastic collisions, the PL peak undergoes a redshift, which is more pronounced compared to surface emission measurements.

A significant shift of the 2.1 eV peak to 1.9 eV at a depth of 12 μm—near the end of the ion range—accompanied by an intensity spike, indicates that the decelerated bismuth ion induces a local deformation field.

The observed PL is extremely sensitive to structural disorder and is presumably associated with the luminescence of aggregate electronic color centers, such as F_2^{2+} centers with a peak emission at 2.2 eV. These centers are typically formed under high fluence conditions due to overlapping ion tracks. The 1.9 eV luminescence spike near the ion stopping range may be related to vacancy creation.

Acknowledgments

This work supported by the Grant (AP09259669) “Radiation resis tance of aluminum-magnesium spinel: optical effects of high-energy ion irradiation” of the Ministry of Science and Education of the Republic of Kazakhstan.

References

[1] K. Yasudaa, T. Yamamotoa, M. Etoh, S. Kawasoea, S. Matsumura, and N. Ishikawa, “Accumulation of radiation damage and disordering in MgAl2O 4 under swift heavy ion irradiation,” Int. J. Mater. Res., vol. 102, no. 9, pp. 1082–1088, 2011, doi: 10.3139/146.110564.

[2] S. Yoshioka et al., “Local structure investigations of accumulated damage in irradiated MgAl2O4,” J. Am. Ceram. Soc., vol. 103, no. 8, pp. 4654–4663, Aug. 2020, doi: 10.1111/JACE.17101.

[3] V. Seeman et al., “Fast-neutron-induced and as-grown structural defects in magnesium aluminate spinel crystals with different stoichiometry,” Opt. Mater. (Amst)., vol. 91, pp. 42–49, May 2019, doi: 10.1016/J.OPTMAT.2019.03.008.

[4] L. Pan, S. Sholom, S. W. S. McKeever, and L. G. Jacobsohn, “Magnesium aluminate spinel for optically stimulated luminescence dosimetry,” J. Alloys Compd., vol. 880, p. 160503, Nov. 2021, doi: 10.1016/J.JALLCOM.2021.160503.

[5] E. Hanamura, Y. Kawabe, H. Takashima, T. Sato, and A. Tomita, “Optical properties of transition-metal doped spinels,” J. Nonlinear Opt. Phys. Mater., vol. 12, no. 4, pp. 467–473, May 2003, doi: 10.1142/S0218863503001584;JOURNAL:JOURNAL:JNOPM;PAGEGROUP:STRING:PUBLICATION.

[6] E. Feldbach et al., “Optical characteristics of virgin and proton-irradiated ceramics of magnesium aluminate spinel,” Opt. Mater. (Amst)., vol. 96, p. 109308, Oct. 2019, doi: 10.1016/J.OPTMAT.2019.109308.

[7] A. Ibarra, D. Bravo, F. J. Lopez, and F. A. Garner, “High-dose neutron irradiation of MgAl2O4 spinel: effects of post-irradiation thermal annealing on EPR and optical absorption,” J. Nucl. Mater., vol. 336, no. 2–3, pp. 156–162, Feb. 2005, doi: 10.1016/J.JNUCMAT.2004.09.003.

[8] A. Lushchik et al., “Creation and thermal annealing of structural defects in neutron-irradiated MgAl2O4 single crystals,” Nucl. Instruments Methods Phys. Res. Sect. B Beam Interact. with Mater. Atoms, vol. 435, pp. 31–37, Nov. 2018, doi: 10.1016/J.NIMB.2017.10.018.

[9] K. Yasuda, T. Yamamoto, M. Shimada, S. Matsumura, Y. Chimi, and N. Ishikawa, “Atomic structure and disordering induced by 350 MeV Au ions in MgAl2O4,” Nucl. Instruments Methods Phys. Res. Sect. B Beam Interact. with Mater. Atoms, vol. 250, no. 1–2, pp. 238–244, Sep. 2006, doi: 10.1016/J.NIMB.2006.04.164.

[10] M. Shimada et al., “Radiation-induced disordering in magnesium aluminate spinel subjected to ionizing radiation,” J. Nucl. Mater., vol. 329–333, no. 1-3 PART B, pp. 1446–1450, Aug. 2004, doi: 10.1016/J.JNUCMAT.2004.04.161.

[11] H. Aizawa, E. Toba, T. Katsumata, S. Komuro, and T. Morikawa, “Characteristics of chromium doped spinel crystals for a fiber-optic thermometer application,” pp. 2976–2979, Dec. 2003, doi: 10.1109/SICE.2002.1195578.

[12] F. Polisadova et al., “Pulse Cathodoluminescence of the Impurity Centers in Ceramics Based on the MgAl2O4 Spinel,” J. Appl. Spectrosc., vol. 85, no. 3, pp. 416–421, Jul. 2018, doi: 10.1007/S10812-018-0666-9/METRICS.

[13] A. Dauletbekova et al., “Depth profiles of aggregate centers and nanodefects in LiF crystals irradiated with 34 MeV 84Kr, 56 MeV 40Ar and 12 MeV 12C ions,” Surf. Coatings Technol., vol. 355, pp. 16–21, Dec. 2018, doi: 10.1016/J.SURFCOAT.2018.03.096.

[14] V. Gritsyna and Y. Kazarinov, “EFFECTS OF TRANSITION-METAL-DOPING ON THE RADIO-LUMINESCENCE PROPERTIES OF MAGNESIUM ALUMINATE SPINEL CRYSTALS,” RAD Assoc. J., vol. 3, no. 1, 2018, doi: 10.21175/RADJ.2018.01.002.

[15] M. Engel, B. Stühn, J. J. Schneider, T. Cornelius, and M. Naumann, “Small-angle X-ray scattering (SAXS) off parallel, cylindrical, well-defined nanopores: From random pore distribution to highly ordered samples,” Appl. Phys. A Mater. Sci. Process., vol. 97, no. 1, pp. 99–108, Oct. 2009, doi: 10.1007/S00339-009-5346-4/METRICS.

Information about authors:
Abdrash Akilbekov – Professor, Doctor of Physical and Mathematical Sciences, Department of Technical Physics, L.N. Gumilyov Eurasian National University, Astana, Kazakhstan, akilbekov_at@enu.kz
Nikita Kirilkin – Master of Engineering, Researcher, Joint Institute for Nuclear Research, Dubna, Russian Federation, kirilkin@jinr.ru
Meruert Mamatova – PhD Student, Engineer, Joint Institute for Nuclear Research, Dubna, Russian Federation, meruert.mamatova@mail.ru

Author Contributions:
Abdrash Akilbekov – concept, methodology, funding acquisition.
Nikita Kirilkin – resources, data collection, testing, modeling.
Meruert Mamatova – analysis, visualization, interpretation, drafting, editing.

Received: *15.05.2025*
Revised: 25.05.2025
Accepted: 28.06.2025
Published: 30.06.2025

Conflict of Interest: The authors declare no conflict of interest.

Use of Artificial Intelligence (AI): The authors declare that AI was not used.